CHAPTER

Non-Cartesian MRI Reconstruction

5

Holger Eggers[,a,*], Melanie Kircheis[**] and Daniel Potts[**]

[*]*Philips Research, Hamburg, Germany* [**]*Technische Universität Chemnitz, Faculty of Mathematics, Chemnitz, Germany*

[a]*Corresponding:* `holger.eggers@philips.com`

ABSTRACT

In this chapter, two fundamental algorithms are introduced for the reconstruction of images from data not sampled on a Cartesian grid in k-space. Such data are routinely collected with methods like echo-planar, periodically rotated overlapping lines with enhanced reconstruction (PROPELLER), radial and spiral imaging. A nonequispaced fast Fourier transform (NFFT) is derived first, which provides an efficient, albeit approximate, conversion between equidistant samples in space and nonequidistant samples in k-space. Gridding is then shown to approximate an inverse NFFT by a weighting of the nonequidistant samples in k-space and an adjoint NFFT, and different approaches to obtaining a suitable weighting are described. Finally, gridding is illustrated with two examples, using an iterative reconstruction based on NFFTs as reference, and aspects of spatial resolution and noise in non-Cartesian imaging are discussed, as well as other NFFTs and their applications.

Keywords: Non-Cartesian MRI, k-space trajectory, NFFT, gridding, sampling density compensation, iterative reconstruction, spatial resolution, signal-to-noise ratio, distortion correction

5.1 INTRODUCTION

Signal localization in MRI is predominantly achieved by superposing onto the strong and homogeneous main magnetic field a comparatively weak magnetic field gradient. The magnetic field gradient ideally produces a linear increase in the magnetic field strength in one direction. Since the frequency of the precession of the nuclear spins,

1

and of the signal this precession induces in the receive coils, is basically proportional to the local magnetic field strength experienced by the nuclear spins, the magnetic field gradient linearly encodes the origin of the signal in the frequency. In this way, the signal is effectively measured in the spatial frequency domain, the so-called k-space.

By allowing rapid changes of the magnetic field gradient in strength and direction over time, MRI provides a remarkable flexibility in sampling k-space. The sampling position $\mathbf{k}$ at time t is simply given by the integral of the magnetic field gradient $\mathbf{G}$ over time

$$\mathbf{k}(t) = \frac{\gamma}{2\pi} \int_0^t \mathbf{G}(\tau) \, d\tau, \tag{5.1}$$

assuming the signal to be generated by radiofrequency excitation at $t = 0$. $\mathbf{k}$ and $\mathbf{G}$ are vectors in typically two-dimensional (2D) or three-dimensional (3D) spaces and are measured in units of $[\mathrm{m}^{-1}]$ and $[\mathrm{T/m}]$, respectively. γ is the gyromagnetic ratio of the concerned nucleus, linking the local magnetic field strength to the angular frequency of the precession. The temporal variation of $\mathbf{G}$, commonly referred to as gradient waveform, thus determines the k-space trajectory, along which samples are collected after a single excitation. It is only restricted by hardware and more fundamentally by safety constraints, which mainly limit the velocity and acceleration in k-space. Using multiple excitations, or shots, permits segmenting the k-space trajectory.

MRI was first demonstrated with projection reconstruction in 1973 [1]. This choice was presumably inspired by CT, with which first clinical images had just been obtained at that time. The data acquisition proceeded along lines through the origin and covered a polar grid in k-space, as illustrated in the bottom left plot in Fig. 5.1. According to the Fourier slice theorem, a one-dimensional (1D) inverse Fourier transform turns the samples along one of these lines into samples of a projection perpendicular to this line. This allowed employing a backprojection for image reconstruction, as in CT.

Two years later, sampling k-space on a Cartesian grid along parallel lines was proposed as a simpler alternative [2]. The application of different magnetic field gradients before and during data acqusition was introduced, establising the distinction between phase and frequency encoding, and the use of a multi-dimensional inverse fast Fourier transform (IFFT) for image reconstruction was suggested. As remarked by one of the authors of this seminal work later, this was driven by the conviction that projections cannot efficiently cover a 2D plane or 3D volume due to the strong variation in sampling density between the center and the periphery of k-space [3]. The combination of sampling k-space on a Cartesian grid and reconstructing images based on an IFFT, known as Cartesian imaging, soon developed into the prevalent method for MRI. In particular in clinical routine, this still holds today.

Nevertheless, a considerable variety of methods has been devised and explored over the last decades that deliberately acquires data not on a Cartesian grid. The
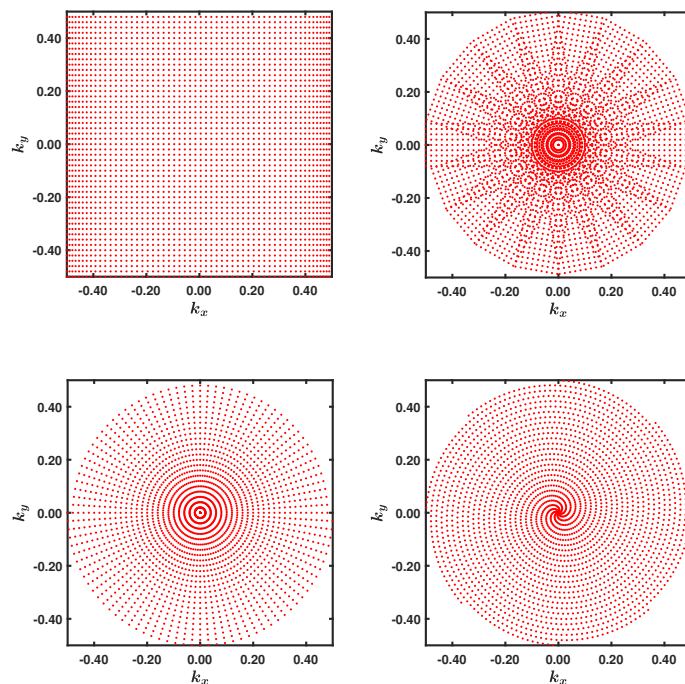
FIGURE 5.1   2D Non-Cartesian Imaging - Sampling Patterns

Nonequidistant sampling of k-space in at least one dimension is involved in 2D echo-planar (top, left), PROPELLER (top, right), radial (bottom, left) and spiral (bottom, right) imaging.

sampling patterns obtained in k-space with four of the most popular of these methods in 2D, including projection reconstruction, are plotted in Fig. 5.1.

Echo-planar imaging (EPI) is often not even considered as a non-Cartesian imaging method [4]. It employs a gradient waveform consisting of a train of trapezoids with alternating polarity for frequency encoding. In its purest form, it traverses the whole k-space after a single excitation along parallel lines in opposite directions. To increase speed and efficiency further, the first samples along each line are aleady collected while the magnetic field gradient is still ramped up and the last samples are still collected while the magnetic field gradient is already ramped down again. This so-called ramp sampling leads to an increasing sampling density towards the edges of k-space in the frequency encoding direction, while a constant sampling density is preserved everywhere else. The sampling is only interrupted for switching between adjacent parallel lines. EPI is in widespread use today, especially for diffusion-weighted imaging (DWI) and functional imaging (fMRI).

Periodically rotated overlapping parallell lines with enhanced reconstruction

4   **CHAPTER 5** Non-Cartesian MRI Reconstruction

(PROPELLER) imaging is also a hybrid Cartesian and non-Cartesian imaging method [5]. The data acquisition is split up into blades, with each of which a rectangular k-space area is covered. Each blade supports an IFFT-based reconstruction of an intermediate image with anisotropic spatial resolution. These intermediate images enable a detection and correction of motion between the acquisition of the individual blades, which are rotated about the k-space origin with respect to each other. However, the reconstruction of the final image has to cope with the highly nonequidistant sampling of k-space by all blades together. PROPELLER imaging is of particular relevance in applications prone to motion, including head, neck, spine, and shoulder imaging.

Radial imaging, or projection reconstruction, is primarily employed in areas in which the strong variation in sampling density between the center and the periphery of k-space actually promises advantages. Above all, the oversampling in the center leads to insensitivity to motion by averaging out inconsistencies in the data to a large extent. Moreover, residual artifacts are spread in two dimensions and appear as streaks, which are usually more benign than the ghosts arising in Cartesian imaging. Additionally, the repeated coverage of the center of k-space enables image reconstruction at various spatial and temporal resolutions in dynamic imaging, as well as retrospective self-gating in abdominal and cardiac imaging during free breathing without interspersed navigators or dedicated sensors. Besides, radial imaging allows dispensing with phase encoding by starting the data acquisition in the center of k-space, permitting very short echo times to capture rapidly decaying signal, as required for lung and bone imaging.

Spiral imaging first and foremost provides a fast and flexible coverage of k-space [6]. It supports single-shot and multi-shot imaging, uniform sampling density in all but the very center of k-space and variable sampling density across k-space, as well as traversing k-space from the center outward and from the periphery inward. Unlike in EPI, the magnetic field gradient continuously changes during the acquisition and dead times for switching its polarity are eliminated. Furthermore, motion and aliasing artifacts are rather incoherent, and especially flow artifacts are less pronounced. Spiral imaging is mainly of interest in a wide range of applications demanding high speed and efficiency, but is very susceptible to an inhomogeneous main magnetic field and an imperfect magnetic field gradient.

All of these 2D methods can be extended to 3D, either by the so-called stacking, the addition of an equidistant sampling along the third dimension, or by a suitable generalization.

Due to the diversity of sampling patterns in MRI, general algorithms are favored for reconstruction in non-Cartesian imaging. In view of the limited signal-to-noise ratio (SNR) typically attainable with MRI, their accuarcy only has to be reasonably good. An essential part of such general algorithms, a nonequispaced fast Fourier transform (NFFT), is described in the next section. Based on it, the ubiquitous gridding is introduced and an iterative reconstruction is outlined in the following sections.

5.2 **NFFT**

The signal s measured in k-space is modeled by

$$s(k) = \int_{-N/2}^{N/2} x(r)\, e^{-i2\pi kr} dr, \tag{5.2}$$

where x denotes the transverse magnetization of an object of maximum extent $[-\frac{N}{2}, \frac{N}{2})$, from now on simply refered to as the object and the field of view (FOV).

A fast Fourier transform (FFT) of length N efficiently converts N equidistant samples of x into N equidistant samples of $\tilde{s}$ defined by

$$\tilde{s}_m = \sum_{n=1}^{N} x_n\, e^{-i2\pi k_m r_n}. \tag{5.3}$$

Here, r and k are unitless and normalized to the range $[-\frac{N}{2}, \frac{N}{2})$ and $[-\frac{1}{2}, \frac{1}{2})$, respectively. Assuming N to be an even positive integer, the sampling positions in space are then located at $r_n = -\frac{N}{2}, -\frac{N}{2} + 1, ..., \frac{N}{2} - 1$. $\tilde{s}$ is linked to s by

$$\tilde{s}(k) = \sum_{p=-\infty}^{\infty} s(k + p) \tag{5.4}$$

due to the limited coverage of k-space by the acquisition and the spatial discretization of the object in the reconstruction. Thus, the $\tilde{s}_m$ in Eq. 5.3 are not samples of s, but of s turned into a periodic signal $\tilde{s}$ with a period of 1. To reduce the computational complexity from $O(N^2)$ of a direct evaluation of Eq. 5.3 to $O(N\log N)$, an FFT exploits symmetries in the exponential factors, which are lost if r_n or k_m are not equidistant anymore.

An NFFT generalizes an FFT to nonequidistant samples of x, $\tilde{s}$, or both [7, 8]. It relies on an FFT for the actual transformation between the spatial and the spatial frequency domain and, therefore, has to convert nonequidistant to equidistant samples intermediately. This involves an approximation, the accuracy of which can be traded off for computational complexity. In the following, the case of equidistant samples of x and nonequidistant samples of $\tilde{s}$ is considered. It is of relevance for an efficient evaluation of Eq. 5.3, the forward model, which requires in non-Cartesian MRI the calculation of M samples of $\tilde{s}$ from N samples of x. The other two cases are discussed at the end of this chapter.

To convert equidistant into nonequidistant samples in k-space, a convolution with a window function c, turned into a periodic function $\tilde{c}$ with a period of 1 by

$$\tilde{c}(k) = \sum_{p=-\infty}^{\infty} c(k + p), \tag{5.5}$$

is performed. $\tilde{c}$ is assumed to have a uniformly convergent Fourier series, which

6   CHAPTER 5 Non-Cartesian MRI Reconstruction

allows writing it as

$$\tilde{c}(k) = \sum_{r=-\infty}^{\infty} \tilde{c}_r \, e^{i2\pi kr} \tag{5.6}$$

with the Fourier coefficients

$$\tilde{c}_r = \int_{-1/2}^{1/2} \tilde{c}(k) \, e^{-i2\pi kr} dk. \tag{5.7}$$

Substituting k by $k - k'$ results in

$$\tilde{c}_r = \int_{-1/2}^{1/2} \tilde{c}(k - k') \, e^{-i2\pi(k-k')r} dk', \tag{5.8}$$

which is approximated by

$$\tilde{c}_r \approx \frac{1}{fN} \sum_{n'=-fN/2}^{fN/2-1} \tilde{c}\left(k - \tfrac{n'}{fN}\right) e^{-i2\pi\left(k-\frac{n'}{fN}\right)r}. \tag{5.9}$$

The oversampling factor $f \geq 1$ is introduced to increase accuracy, where fN is also assumed to be an even positive integer [9, 10]. If the periodic function $\tilde{c}$ is bandlimited with a maximum frequency of $\frac{fN}{2}$, Eq. 5.9 holds exactly. Otherwise, aliasing occurs and the estimation of the $\tilde{c}_r$ is confounded by higher frequencies. More specifically, the frequency bands $[fNp - \frac{N}{2}, fNp + \frac{N}{2})$, for any integer $p \neq 0$, fold back onto the baseband $[-\frac{N}{2}, \frac{N}{2})$. Rearranging Eq. 5.9 leads to

$$e^{i2\pi kr} \approx \frac{1}{fN\tilde{c}_r} \sum_{n'=-fN/2}^{fN/2-1} \tilde{c}\left(k - \tfrac{n'}{fN}\right) e^{i2\pi \frac{n'}{fN}r}, \tag{5.10}$$

provided that $\tilde{c}_r \neq 0$, and substituting r by $-r$ to

$$e^{-i2\pi kr} \approx \frac{1}{fN\tilde{c}_{-r}} \sum_{n'=-fN/2}^{fN/2-1} \tilde{c}\left(k - \tfrac{n'}{fN}\right) e^{-i2\pi \frac{n'}{fN}r}, \tag{5.11}$$

which is inserted into Eq. 5.3 to obtain

$$\tilde{s}_m \approx \sum_{n'=-fN/2}^{fN/2-1} \tilde{c}\left(k_m - \tfrac{n'}{fN}\right) \sum_{n=1}^{N} \frac{x_n}{fN\tilde{c}_{-r_n}} e^{-i2\pi \frac{n'}{fN}r_n}. \tag{5.12}$$

The inner sum amounts to an FFT of length fN, transforming N equidistant samples of x in space, after weighting and zero padding to fN equidistant samples in space, into fN equidistant samples in k-space. The outer sum converts the latter by a convolution into M nonequidistant samples in k-space.

Choosing

$$\tilde{c}_r = \begin{cases} \frac{1}{fN}, & -\frac{fN}{2} < r \leq \frac{fN}{2} \\ 0, & \text{otherwise} \end{cases} \tag{5.13}$$

allows dispensing with the weighting, usually referred to as deapodization, and results with Eq. 5.6 in

$$\tilde{c}(k) = \frac{1}{fN} \sum_{r=-fN/2+1}^{fN/2} e^{i2\pi kr}. \tag{5.14}$$

Here, the shift in the range of r arises from substituting r by $-r$ above. $\tilde{c}(k)$ is a complex trigonometric polynomial of degree $\frac{fN}{2}$ in this case, for which Eq. 5.9 holds exactly. It is written as

$$\tilde{c}(k) = \frac{\sin(\pi k fN)}{fN \sin(\pi k)} e^{i\pi k} \tag{5.15}$$

and approximated by

$$\tilde{c}(k) \approx \text{sinc}(\pi k fN) \tag{5.16}$$

for small πk using

$$\text{sinc}(x) = \begin{cases} \frac{\sin(x)}{x}, & x \neq 0 \\ 1, & \text{otherwise} \end{cases}. \tag{5.17}$$

According to the sampling theorem, s can be recovered from equidistant samples of s by

$$s(k) = \sum_{n=-\infty}^{\infty} s\left(\frac{n}{fN}\right) \text{sinc}\left(\pi \left(k - \frac{n}{fN}\right) fN\right). \tag{5.18}$$

Consequently, the sinc function of infinite extent is the ideal window function in the hypothetical case of unlimited coverage of k-space by the acquisition. In the practicable case of limited coverage of k-space, however, it is, according to Eq. 5.15, better replaced by the sinc function turned into a periodic function, times the phasor $e^{i\pi k}$, which arises from the asymmetry in r_n for even fN.

To reduce the computational complexity of the convolution, the window function is preferably real and limited in its extent, either by design or by truncation, to $[-\frac{K}{2fN}, \frac{K}{2fN}]$ with a positive integer K, the kernel size. A truncation leads to

$$c'(k) = \begin{cases} c(k), & |k| \leq \frac{K}{2fN} \\ 0, & \text{otherwise} \end{cases} \tag{5.19}$$

and a corresponding periodic function $\tilde{c}'$ with a period of 1, and changes Eq. 5.12 to

$$\tilde{s}_m \approx \sum_{n'=-fN/2}^{fN/2-1} \tilde{c}'\left(k_m - \frac{n'}{fN}\right) \sum_{n=1}^{N} \frac{x_n}{fN\tilde{c}_{-r_n}} e^{-i2\pi \frac{n'}{fN} r_n}. \tag{5.20}$$

8   **CHAPTER 5** Non-Cartesian MRI Reconstruction

The Kaiser-Bessel window is, in the continuous case, a simple approximation to prolate spheroidal wave functions, which maximize the relative energy of a function of given extent in one domain in an interval of given extent in the other domain [11, 12]. Thus, it is particularly well suited to minimize aliasing errors in Eq. 5.12 and truncation errors in Eq. 5.20 [10, 13]. If aliasing errors are to be minimized, the deapodization is defined by the Kaiser-Bessel window

$$\tilde{c}_r = \begin{cases} \frac{1}{fN} I_0\left(b\sqrt{1 - \left(\frac{\pi K}{fNb}r\right)^2}\right), & |r| \leq \frac{fNb}{\pi K} \\ 0, & \text{otherwise} \end{cases}, \tag{5.21}$$

where I_0 is the zeroth order modified Bessel function of the first kind. By setting the shape parameter b to

$$b = \pi K\left(1 - \frac{1}{2f}\right), \tag{5.22}$$

the Fourier coefficients drop to zero for $|r| > fN - \frac{N}{2}$ [14]. The window function, also referred to as convolution kernel, is then given by

$$c(k) = \begin{cases} \frac{2b}{\pi K}\text{sinhc}\left(b\sqrt{1 - \left(\frac{2fN}{K}k\right)^2}\right), & |k| \leq \frac{K}{2fN} \\ \frac{2b}{\pi K}\text{sinc}\left(b\sqrt{\left(\frac{2fN}{K}k\right)^2 - 1}\right), & \text{otherwise} \end{cases} \tag{5.23}$$

using

$$\text{sinhc}(x) = \begin{cases} \frac{\sinh(x)}{x}, & x \neq 0 \\ 1, & \text{otherwise} \end{cases}. \tag{5.24}$$

If truncation errors are to be minimized instead, the convolution kernel is defined by the Kaiser-Bessel window

$$c(k) = \begin{cases} \frac{1}{K} I_0\left(b\sqrt{1 - \left(\frac{2fN}{K}k\right)^2}\right), & |k| \leq \frac{K}{2fN} \\ 0, & \text{otherwise} \end{cases} \tag{5.25}$$

and the deapodization is given by

$$\tilde{c}_r = \begin{cases} \frac{1}{fN}\text{sinhc}\left(b\sqrt{1 - \left(\frac{\pi K}{fNb}r\right)^2}\right), & |r| \leq \frac{fNb}{\pi K} \\ \frac{1}{fN}\text{sinc}\left(b\sqrt{\left(\frac{\pi K}{fNb}r\right)^2 - 1}\right), & \text{otherwise} \end{cases}. \tag{5.26}$$

Both choices lead to similar convolution kernels and deapodizations, as illustrated in Fig. 5.2 and Fig. 5.3 with $f = 2.0$, $K = 5$, $N = 800$, and a normalization of the values of the functions to the range $[0, 1]$. It is worth noting that the second case in Eq. 5.23 and Eq. 5.26 is just provided for completeness. Due to the truncation of the convolution kernel and the limited extent of the object, only the first case is of relevance in practice. Moreover, by subtracting an offset of $\frac{1}{fN}I_0(b)$ and $\frac{1}{K}I_0(b)$ from
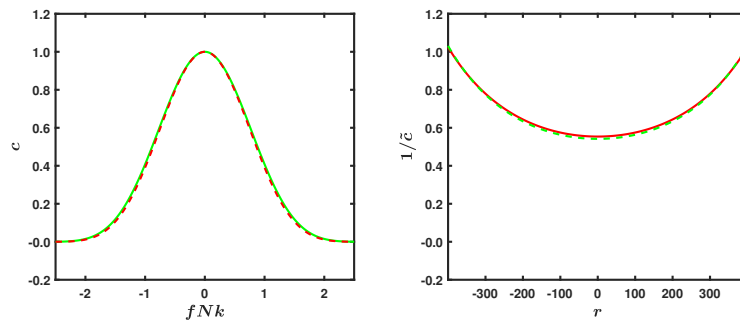
FIGURE 5.2   Convolution Kernels and Deapodizations

A Kaiser-Bessel window is employed as convolution kernel in the conversion of equidistant into nonequidistant samples in k-space (red, left). To compensate for the inherent low-pass filtering, a deapodization is performed in space by dividing by the inverse Fourier transform of the Kaiser-Bessel window (red, right). Alternatively, dividing by a Kaiser-Bessel window serves the deapodzation (green, right) and the Fourier transform of the Kaiser-Bessel window as convolution kernel (green, left).

the first case of Eq. 5.21 and Eq. 5.25, the Kaiser-Bessel window smoothly drops to zero already at $|r| = \frac{fNb}{\pi K}$ and $|k| = \frac{K}{2fN}$, which allows eliminating aliasing errors and preventing the convolution kernel from extending over $K + 1$ equidistant samples in k-space in the worst case, respectively.

In general, the accuracy and the computational complexity of an NFFT increase with increasing oversampling factor and kernel size. Error bounds have been established for various window functions to guide the selection of minimal values for f and K given a target accuracy [8]. Since the running time of an FFT is usually not a monotonic function of the length of the FFT, the choice of f is preferably made in view of the running time of an FFT of length fN [15]. The complexity of the window function is less of a concern, because it is typically calculated only once and stored in a look-up table [16].

Eq. 5.20 can be rewritten as

$$\tilde{\mathbf{s}} \approx \mathbf{C}' \, \mathbf{F} \, \mathbf{D} \, \mathbf{x} \tag{5.27}$$

with a diagonal N x N deapodization matrix $\mathbf{D}$

$$[\mathbf{D}]_{n,n} = \frac{1}{fN\tilde{c}_{-r_n}}, \tag{5.28}$$

an fN x N Fourier transform matrix $\mathbf{F}$

$$[\mathbf{F}]_{n',n} = \mathrm{e}^{-\mathrm{i}2\pi\left(\frac{n'-1}{fN} - \frac{1}{2}\right)r_n}, \tag{5.29}$$

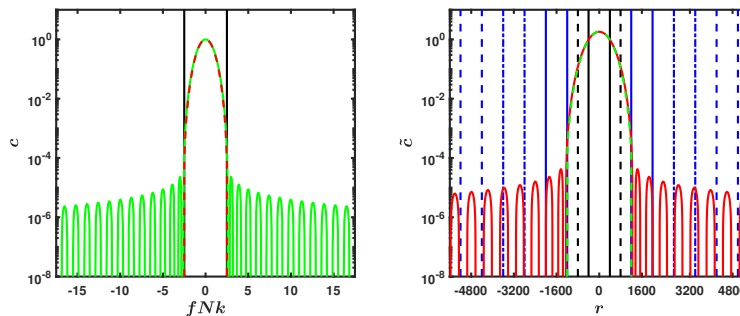**10** **CHAPTER 5** Non-Cartesian MRI Reconstruction

FIGURE 5.3   Aliasing and Truncation Errors

The convolution kernels from Fig. 5.2 and their inverse Fourier transforms are displayed with a logarithmic scale over a larger range of k and r, respectively. While a Kaiser-Bessel window is a function with compact support, its Fourier transform and inverse Fourier transform are not. Consequently, aliasing errors occur in space using a Kaiser-Bessel window as convolution kernel in k-space (red, right), whereas truncation errors occur in k-space using it for deapodization in space (green, left). The prescribed kernel size and FOV (solid black), the FOV extended by oversampling (dashed black), and the first three frequency bands folding back onto the prescribed FOV (solid, dashdotted, and dashed blue) are indicated.

and a sparse M x fN convolution matrix $\mathbf{C}'$

$$[\mathbf{C}']_{m,n'} = \tilde{c}'\left(k_m - \frac{n'-1}{fN} + \frac{1}{2}\right). \tag{5.30}$$

Here, the entries in the columns and rows of the matrices are numbered starting at 1, which complicates the expressions in the parentheses in Eq. 5.29 and Eq. 5.30 compared to Eq. 5.20. Eq. 5.27 is an approximation of

$$\tilde{\mathbf{s}} = \mathbf{E}\,\mathbf{x} \tag{5.31}$$

with an M x N encoding matrix $\mathbf{E}$

$$[\mathbf{E}]_{m,n} = \mathrm{e}^{-\mathrm{i}2\pi k_m r_n}. \tag{5.32}$$

Extending an NFFT to multiple dimensions is straightforward using a tensor product approach. While separable convolution kernels, defined by the product of 1D convolution kernels for each dimension, are convenient and prevailing in practice, non-separable convolution kernels, such as circularly and spherically symmetric ones, promise to enhance accuracy given a target computational complexity [17]. However, a theoretical comparison of them still seems to be missing.

5.3 GRIDDING

The object x is ideally recovered from the signal s by

$$x(r) = \int_{-\infty}^{\infty} s(k)\, e^{i2\pi kr} dk. \tag{5.33}$$

Due to the limited coverage of k-space by the acquisition, s is only known for k in $[-\frac{1}{2}, \frac{1}{2})$ and, without prior knowledge, disregarded elsewhere, which leads to the approximation

$$\hat{x}(r) = \int_{-1/2}^{1/2} s(k)\, e^{i2\pi kr} dk. \tag{5.34}$$

In addition, s is sampled with finite resolution, limited by hardware constraints in the frequency encoding direction and more fundamentally by time constraints in the phase encoding direction(s), resulting in the further approximation

$$\hat{x}_n = \frac{1}{M} \sum_{m=1}^{M} s_m\, e^{i2\pi k_m r_n} \tag{5.35}$$

or

$$\hat{\mathbf{x}} = \frac{1}{M} \mathbf{E}^{\mathrm{H}} \mathbf{s}. \tag{5.36}$$

An IFFT of length M efficiently converts M equidistant samples of s into M equidistant samples of $\hat{x}$. If the object is to be reconstructed with higher spatial resolution, that is to be enlarged by Fourier interpolation, the number of equidistant samples of $\hat{x}$, and with it the length of the IFFT, is increased here to $N > M$, whereas the spacing of the equidistant samples of s is decreased to $\frac{1}{N}$. In analogy with Eq. 5.14 and Eq. 5.15, the point spread function (PSF), which links x to $\hat{x}$, is then given by

$$\begin{aligned}
\mathrm{PSF}(r) &= \frac{1}{N} \sum_{m=-M/2}^{M/2-1} e^{i2\pi \frac{m}{N} r} \\
&= \frac{\sin\left(\pi M \frac{r}{N}\right)}{N \sin\left(\pi \frac{r}{N}\right)} e^{-i\pi \frac{r}{N}}.
\end{aligned} \tag{5.37}$$

Thus, the equidistant samples of $\hat{x}$ are approximately related by a sinc interpolation. Only in the case of $N = M$, which is exceptional because Fourier interpolation is almost always applied in clinical routine, they are uncorrelated.

An IFFT is both the adjoint and the inverse of the corresponding FFT. For an NFFT, this does not hold anymore. Gridding was developed in radioastronomy from simpler interpolation methods and adopted in medical imaging before NFFTs were proposed and thoroughly analyzed in mathematics [18, 9]. It aims at reconstructing

N equidistant samples of x from M nonequidistant samples of s. To provide an approximate explicit inverse NFFT (INFFT), gridding relies on an adjoint NFFT and introduces an additional weighting of the nonequidistant samples of s, the sampling density compensation. It is described by

$$\hat{\mathbf{x}} \approx \mathbf{D}^H \mathbf{F}^H \mathbf{C}'^H \mathbf{W} \mathbf{s} \tag{5.38}$$

with a M x M diagonal matrix $\mathbf{W}$ of a vector of weights $\mathbf{w}$.

Different approaches to deriving a suitable sampling density compensation have been proposed. One class of them considers each s_m as representative for a certain neighborhood in k-space and turns Eq. 5.35 into the Riemann sum

$$\hat{x}_n = \sum_{m=1}^{M} w_m s_m \, e^{i2\pi k_m r_n}. \tag{5.39}$$

Here, the sum of the positive weights, which represent lengths in 1D, is normalized to a value of 1. The calculation of the weights is based on either a continuous or a discrete model.

For simple non-Cartesian sampling patterns, the weights can analytically be obtained from the Jacobian determinant of a differentiable coordinate transformation to a Cartesian sampling pattern. In the case of 2D radial imaging, the coordinate transformation from a polar grid to a Cartesian grid is defined by

$$k_x = k_r \cos\left(2\pi k_\phi\right)$$
$$k_y = k_r \sin\left(2\pi k_\phi\right) \tag{5.40}$$

with the radial direction k_r and the azimuthal direction k_ϕ normalized to the range $[0, \frac{1}{2}]$ and $[-\frac{1}{2}, \frac{1}{2})$, respectively. The determinant of the Jacobian matrix

$$J_R = \begin{bmatrix} \frac{\partial k_x}{\partial k_r} & \frac{\partial k_x}{\partial k_\phi} \\ \frac{\partial k_y}{\partial k_r} & \frac{\partial k_y}{\partial k_\phi} \end{bmatrix} \tag{5.41}$$

is then equal to $2\pi k_r$. Extending the integration in Eq. 5.34 to a circular area R of radius $\frac{1}{2}$ in 2D results in

$$\hat{x}(r_x, r_y) = \iint\limits_{R} s\left(k_x, k_y\right) e^{i2\pi\left(k_x r_x + k_y r_y\right)} dk_x dk_y \tag{5.42}$$

and a change in variables in

$$\hat{x}(r_x, r_y) = 2\pi \int_{0}^{1/2} \int_{-1/2}^{1/2} s\left(k_r, k_\phi\right) k_r \, e^{i2\pi k_r\left(\cos\left(2\pi k_\phi\right) r_x + \sin\left(2\pi k_\phi\right) r_y\right)} dk_\phi dk_r. \tag{5.43}$$

Accordingly, $s(k_r, k_\phi)$ is weighted by $2\pi k_r$, which corresponds to the ideal ramp filter used in backprojection.

In the case of 2D spiral imaging, a coordinate transformation to a polar grid exists

for some common k-space trajectories, which can readily be extended to a coordinate transformation to a Cartesian grid [19]. For the segmented, or interleaved, variable angular speed k-space trajectory plotted in Fig. 5.1 on the bottom right, it is defined by

$$
\begin{aligned}
k_r &= \frac{k_s}{2\sqrt{\alpha + (1-\alpha)\,k_s}} \\
k_\phi &= \frac{N}{2M_I} \cdot \frac{k_s}{\sqrt{\alpha + (1-\alpha)\,k_s}} + k_i,
\end{aligned}
\tag{5.44}
$$

where k_s parameterizes the sample, or time, along an interleaf, normalized to the range $[0, 1]$, and k_i parameterizes the interleaf, or its rotation around the k-space origin, normalized to the range $[-\frac{1}{2}, \frac{1}{2})$. Both k_s and k_i are considered as continuous here. The range of k_ϕ is extended to $[-\frac{1}{2}, \frac{1}{2} + \frac{N}{2M_I})$, and M is subdivided into M_I interleaves with M_S samples each. Since

$$
k_r = \frac{M_I}{N}\left(k_\phi - k_i\right),
\tag{5.45}
$$

this is an Archimedean spiral with a parameter α in the range $[0, 1]$. For $\alpha = 0$ and $\alpha = 1$, a constant linear velocity spiral and a constant angular velocity spiral is obtained, respectively. The determinant of the Jacobian matrix

$$
J_S = \begin{bmatrix} \frac{\partial k_r}{\partial k_s} & \frac{\partial k_r}{\partial k_i} \\ \frac{\partial k_\phi}{\partial k_s} & \frac{\partial k_\phi}{\partial k_i} \end{bmatrix}
\tag{5.46}
$$

is then given by

$$
|J_S| = \frac{2\alpha + (1-\alpha)\,k_s}{4\left(\alpha + (1-\alpha)\,k_s\right)^{\frac{3}{2}}}
\tag{5.47}
$$

and the determinant of the Jacobian matrix of the composite coordinate transformation to a Cartesian grid by

$$
|J_S\,J_R| = \frac{\pi}{4} \cdot \frac{2\alpha k_s + (1-\alpha)\,k_s^2}{\left(\alpha + (1-\alpha)\,k_s\right)^2}.
\tag{5.48}
$$

For more complex non-Cartesian sampling patterns, the weights can geometrically be obtained from the discrete k-space sampling positions, constructing a Voronoi diagram and calculating the area of each Voronoi cell, for instance [20].

Another class of approaches solves a minimization problem. For example, replacing $\mathbf{s}$ in Eq. 5.38 by $\tilde{\mathbf{s}}$ from Eq. 5.27 leads to

$$
\hat{\mathbf{x}} \approx \mathbf{D}^H\,\mathbf{F}^H\,\mathbf{C}'^H\,\mathbf{W}\,\mathbf{C}'\,\mathbf{F}\,\mathbf{D}\,\mathbf{x}.
\tag{5.49}
$$

Setting $\mathbf{D} = \mathbf{I}$ eliminates the deapodization and turns the sparse convolution matrix $\mathbf{C}'$ into a dense convolution matrix $\mathbf{C}$. Choosing additionally $f = 1.0$ allows simpli-

fying Eq. 5.49 to

$$\mathbf{F}\hat{\mathbf{x}} \approx N\,\mathbf{C}^{H}\,\mathbf{W}\,\mathbf{C}\,\mathbf{F}\,\mathbf{x},\qquad(5.50)$$

since $\mathbf{F}\,\mathbf{F}^{H} = N\,\mathbf{I}$. Ideally, applying the forward model to an image and then gridding to the simulated signal recovers the image. Independent of $\mathbf{x}$, this would be ensured by the condition

$$N\,\mathbf{C}^{H}\,\mathbf{W}\,\mathbf{C} = \mathbf{I}.\qquad(5.51)$$

However, this matrix equation is normally overdetermined. It can be rewritten as a linear system of N^2 equations and multiplied on the left with the system matrix, or the Frobenius norm of the matrix $N\,\mathbf{C}^{H}\,\mathbf{W}\,\mathbf{C} - \mathbf{I}$ can be minimized instead [21, 22]. Both lead to the same linear system of M equations

$$\mathbf{A}\,\mathbf{w} = \mathbf{b}\qquad(5.52)$$

with

$$[\mathbf{A}]_{m,m'} = \left|\left[\mathbf{C}\,\mathbf{C}^{H}\right]_{m,m'}\right|^{2}$$
$$[\mathbf{b}]_{m} = \frac{1}{N}\left[\mathbf{C}\,\mathbf{C}^{H}\right]_{m,m}.\qquad(5.53)$$

Due to the often poor condition and the high computational complexity, solving Eq. 5.52 is only practicable for non-Cartesian sampling patterns with smaller number of samples. It is worth noting that the weights obtained by this least squares approximation of Eq. 5.51 are not necessarily positive anymore.

Similarly,

$$N\,\mathbf{C}\,\mathbf{C}^{H}\,\mathbf{W} = \mathbf{I}\qquad(5.54)$$

is derived by demanding consistency of the signal in k-space rather than of the image in space. If this condition is relaxed by considering the diagonal elements of the resulting matrices on the left and on the right only, it reduces to

$$N\,\mathbf{C}\,\mathbf{C}^{H}\,\mathbf{w} = \mathbf{1},\qquad(5.55)$$

for the solution of which the fix-point iteration

$$\left[\mathbf{w}^{[i+1]}\right]_{m} = \frac{\left[\mathbf{w}^{[i]}\right]_{m}}{N\left[\mathbf{C}\,\mathbf{C}^{H}\mathbf{w}^{[i]}\right]_{m}}\qquad(5.56)$$

was suggested, which remains practicable for non-Cartesian sampling patterns with higher number of samples using a truncated convolution kernel [23].

A generalization of gridding is obtained by replacing the sampling density compensation with a spatially variant convolution kernel, promising better accuracy at the expense of higher computational complexity for optimizing the convolution kernel once per sampling pattern [22].

5.4 **ITERATIVE RECONSTRUCTION**

Replacing $\tilde{\mathbf{s}}$ by $\mathbf{s}$ in Eq. 5.31 leads to the forward model

$$\mathbf{s} = \mathbf{E}\,\mathbf{x}. \tag{5.57}$$

The inverse problem is solved by the least squares approximation

$$\min_{\hat{\mathbf{x}}} \|\mathbf{s} - \mathbf{E}\,\hat{\mathbf{x}}\|_2^2 \tag{5.58}$$

using the normal equations of the first kind

$$\mathbf{E}^{\mathrm{H}}\,\mathbf{E}\,\hat{\mathbf{x}} = \mathbf{E}^{\mathrm{H}}\,\mathbf{s}, \tag{5.59}$$

or by the weighted least squares approximation

$$\min_{\hat{\mathbf{x}}} \sum_{m=1}^{M} [\mathbf{w}]_m \, |[\mathbf{s} - \mathbf{E}\,\hat{\mathbf{x}}]_m|^2 \tag{5.60}$$

using the modified normal equations of the first kind

$$\mathbf{E}^{\mathrm{H}}\,\mathbf{W}\,\mathbf{E}\,\hat{\mathbf{x}} = \mathbf{E}^{\mathrm{H}}\,\mathbf{W}\,\mathbf{s}. \tag{5.61}$$

Here, Eq. 5.57 is assumed to be overdetermined, and the diagonal matrix $\mathbf{W}$ of the vector $\mathbf{w}$ is specifically the one introduced for sampling density compensation.

Iterative methods, such as the conjugate gradient (CG) method, are preferably applied to the large linear system of equations Eq. 5.59 and Eq. 5.61. They typically involve a repeated calculation of products of the system matrix $\mathbf{E}^{\mathrm{H}}\,\mathbf{E}$ or $\mathbf{E}^{\mathrm{H}}\,\mathbf{W}\,\mathbf{E}$ and a vector $\hat{\mathbf{p}}$. These products can efficiently be computed either with an NFFT and an adjoint NFFT or with a fast convolution [24]. For the latter, the entries of the system matrix are written as

$$\left[\mathbf{E}^{\mathrm{H}}\,\mathbf{E}\right]_{n,n'} = \sum_{m=1}^{M} \mathrm{e}^{\mathrm{i}2\pi k_m(r_n - r_{n'})} \tag{5.62}$$

or

$$\left[\mathbf{E}^{\mathrm{H}}\,\mathbf{W}\,\mathbf{E}\right]_{n,n'} = \sum_{m=1}^{M} w_m \, \mathrm{e}^{\mathrm{i}2\pi k_m(r_n - r_{n'})} \tag{5.63}$$

and refered to as $q\,(r_n - r_{n'})$. It is worth noting that $q(r)$ corresponds to the PSF for a reconstruction with an adjoint NFFT or a gridding. The products then reduce to the convolution

$$\sum_{n'=1}^{N} \hat{p}_{n'}\, q\,(r_n - r_{n'}) \tag{5.64}$$

in space, which can be evaluated by a multiplication in k-space. In this way, an NFFT and an adjoint NFFT are essentially replaced by an FFT and an IFFT. The
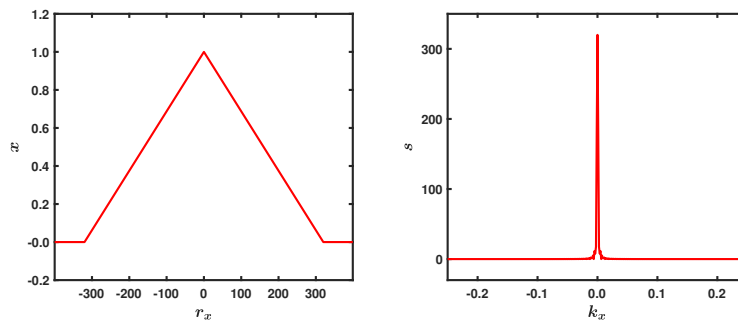
FIGURE 5.4   1D Object

A continuous triangular function, covering 80% of the FOV, is chosen as 1D object (left). Its frequency spectrum is real and non-negative (right).

Fourier transform of q has to be computed only once. However, the fast convolution requires a two-fold oversampling to prevent backfolding. In the overdetermined case, it usually provides a substantial acceleration nevertheless [25].

Iterative methods can synthesize signal outside the k-space area covered by the acquisition [26]. This concerns in particular the edges of a square k-space, if only the circle inscribed in the square is actually sampled. Since recovering such signal is ill-conditioned, it typically entails an excessive noise amplification. To suppress the resulting high-frequency noise, a low-pass filtering is usually applied to the reconstructed image.

5.5 EXAMPLES

Gridding is first illustrated with a 1D example, in which the triangular function shown in Fig. 5.4 serves as object. The Fourier transform of this object is given by

$$s(k_x) = R \operatorname{sinc}^2(\pi R k_x), \tag{5.65}$$

where $R = 320$.

Initially, an equidistant sampling of s with k_x in the range $[-\frac{1}{4}, \frac{1}{4})$ and $M = 400$ is assumed. The object is reconstructed at $r_x = -\frac{N}{2}, ..., \frac{N}{2} - 1$ with $N = 800$. Thus, it is enlarged by Fourier interpolation by a factor of 2, involving zero padding in k-space to the range $[-\frac{1}{2}, \frac{1}{2})$. The equidistant sampling allows applying an IFFT for reference and assessing truncation or aliasing errors introduced by a gridding. Resulting errors are plotted in Fig. 5.5 and are dominated by ringing artifacts at $r_x = -320, 0, 320$. The triangular function is continuous but not differentiable at these points. Therefore, the classical Gibbs phenomenon is not observed, but a poorer approximation by a
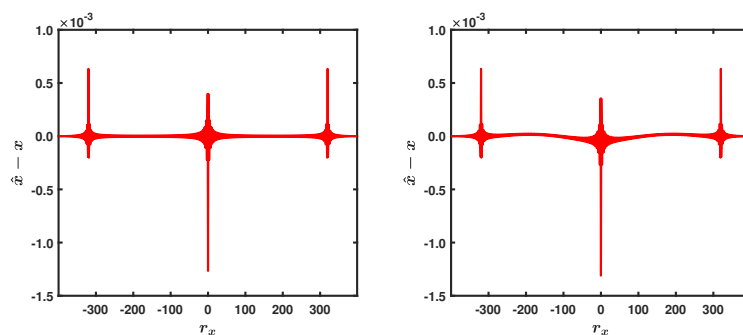
FIGURE 5.5   1D Cartesian Sampling - IFFT versus Gridding

From an equidistant sampling of the frequency spectrum in Fig. 5.4, 1D objects are reconstructed with twice the spatial resolution using zero padding, once with an IFFT (left) and once with a gridding (right), and the errors to the continuous triangular function are calculated.

truncated Fourier series is expected due to the slower decay of the Fourier coefficients with frequency. Compared to the IFFT, the gridding with $f = 2$ and $K = 5$ adds only negligible errors, which originate from the truncation of the convolution kernel in this case. In the following, these settings of the oversampling factor and the kernel size are kept.

To simulate a nonequidistant sampling of s, the readout gradient is assumed to ramp up $100\,\mu$s after the excitation with a gradient slew rate of $200\,\text{Tm}^{-1}\text{s}^{-1}$, at which point in time the data acquisition is also triggered, and to level off at a gradient strength of $40\,\text{Tm}^{-1}$, as illustrated in Fig. 5.6. The gradient system is modeled as a linear time-invariant system, once with an ideal frequency response

$$H(\mathrm{i}\omega) = 1 \qquad (5.66)$$

and once with a more realistic frequency response

$$H(\mathrm{i}\omega) = \frac{\mathrm{e}^{\mathrm{i}\omega T}}{1 + \mathrm{i}\omega T}, \qquad (5.67)$$

which corresponds to a mono-exponential decay with a time constant T, chosen to be $40\,\mu$s in this example. The amplitude and phase of $H(\mathrm{i}\omega)$ are plotted in Fig. 5.7. In the ideal case, the actual gradient waveform is identical with the demand gradient waveform. In the more realistic case, however, the actual gradient waveform is smoothed. This is seen in Fig. 5.6, as well as the resulting k-space sampling positions as function of time. The data acquisition is performed twice, with positive and negative polarity of the readout gradient, to traverse the 1D k-space from the center, or origin, to the periphery, in positive and negative direction, respectively. Thus, the same range of k_x as before is covered. The sampling positions are located
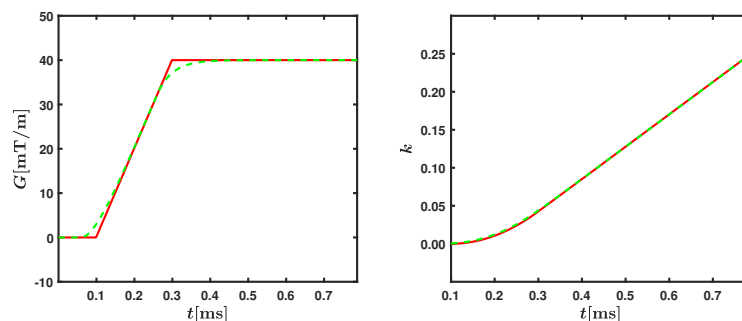
FIGURE 5.6   Gradient Waveform and k-Space Trajectory

The demand gradient waveform (red, left) increases linearly with the maximum gradient slew rate until the maximum gradient strength is reached. The real gradient system from Fig. 5.7 low-pass filters the gradient waveform (green, left), leading to a distortion of the k-space trajectory hardly perceptible at this scale (right).
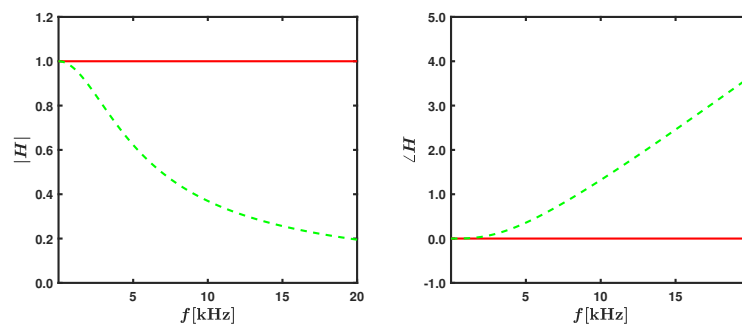

FIGURE 5.7   Gradient System Characterization

An ideal gradient system (red) has an invariant amplitude (left) and phase (right) response, whereas a real gradient system (green) typically exhibits an amplitude response decaying with frequency and a phase response growing with frequency.

at the points of intersection of the horizontal black lines ($k_y = 0$) with the colored circles in Fig. 5.8. While the sampling density in principle increases towards the k-space center, $|k_x| < \frac{0.36}{N}$ remains uncovered in the case of the more realistic gradient system. It is worth noting that this does not constitute an undersampling per se, because the critical sampling distance of $\frac{1}{N}$ is larger than the diameter of the gap.

Applying a gridding to the nonequidistant sampling of s produces the errors plotted in Fig. 5.9. With the ideal gradient system, a moderate offset is observed, whereas
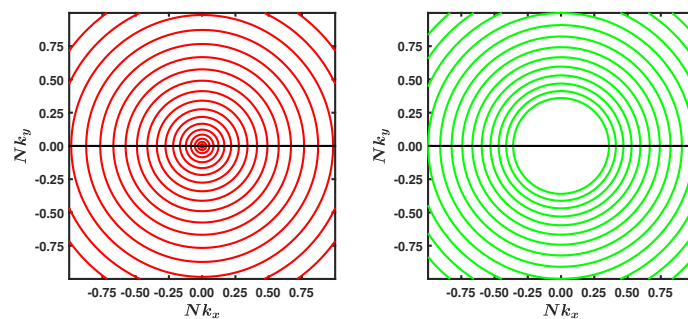
FIGURE 5.8   1D and 2D Sampling Patterns

From the k-space trajectories in Fig. 5.6, 1D (k_x) and 2D (k_x, k_y) sampling patterns are generated by equiangular rotation around the origin. Unlike with the ideal gradient system (left), the sampling pattern obtained with the more realistic gradient system (right) leaves a gap in the k-space center, which is enlarged in both graphs.
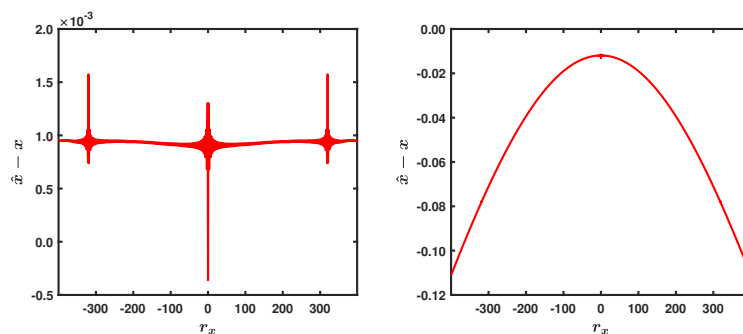

FIGURE 5.9   1D Non-Cartesian Sampling - Gridding

Using the two nonequidistant 1D sampling patterns from Fig. 5.8, 1D objects are reconstructed with twice the spatial resolution with a gridding and the errors to the continuous triangular function are calculated.

with the more realistic gradient system, major errors apparently arise from the central gap in the sampling pattern.

So far, a sampling density compensation based on the distance between adjacent k-space sampling positions has been used. Weights obtained with this geometrical approach and with some of the other approaches described above are juxtaposed in Fig. 5.10, along with corresponding errors, for the problematic case of the more realistic gradient system. The fix-point iteration according to Eq. 5.56 slowly converges from $\mathbf{w}^{[0]} = \frac{1}{N} \mathbf{1}$, for which the weights always remain positive. A sinc^2 con-

20   **CHAPTER 5** Non-Cartesian MRI Reconstruction
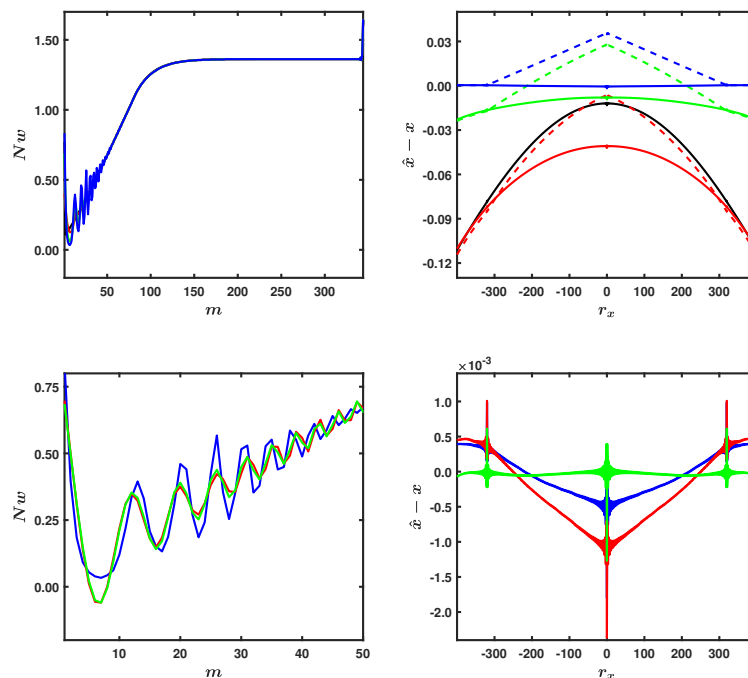

FIGURE 5.10   Sampling Density Compensation

From the second nonequidistant 1D sampling pattern in Fig. 5.8, weights for sampling density compensation are derived (left), geometrically (top, black), numerically based on a repeated gridding with 5 (top, red), 25 (top, green), and 125 (top and bottom, blue) iterations, once with (solid) and once without (dashed) normalization, and algebraically based on Eq. 5.55 (bottom, red) and Eq. 5.52 (bottom, green). 1D objects are reconstructed with them and the errors to the continuous triangular function are calculated (right).

volution kernel, truncated to two side lobes, was employed in this example to map nonequidistant samples to nonequidistant samples directly [27]. Errors decrease at first, but soon are dominated by a systematic overestimation of the weights due to the omitted side lobes. By contrast, enforcing $\|\mathbf{w}\|_1 = 1$ allows reducing errors by two orders of magnitude overall, yet results deteriorate again when proceeding with the iteration. Solving Eq. 5.55 and Eq. 5.52 leads to weights that still show the striking, unexpected oscillation for the sampling positions close to the k-space center, but that are not necessarily positive anymore. The same convolution kernel as before was chosen in the first case, while Eq. 5.15 was selected in the second case. A CG method without explicit regularization reliably converges only in the second case, in which also the lowest errors are attained.
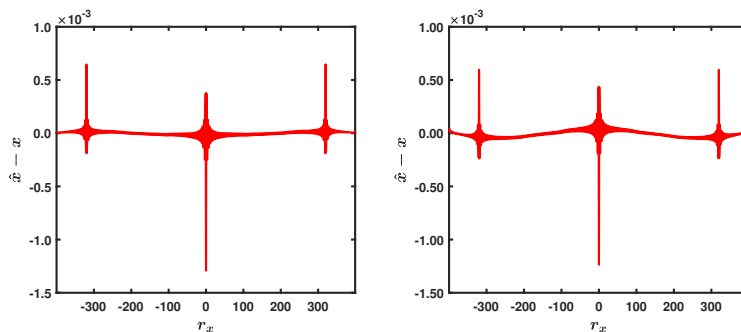
FIGURE 5.11   1D Non-Cartesian Sampling - Iterative Reconstruction

Using the two nonequidistant 1D sampling patterns from Fig. 5.8, 1D objects are iteratively reconstructed with twice the spatial resolution and the errors to the continuous triangular function are calculated.

Finally, results obtained with an iterative reconstruction are provided for reference in Fig. 5.11. A CG method, initialized with $\hat{\mathbf{x}}^{[0]} = \mathbf{0}$, leads to similar errors as a gridding in the case of equidistant sampling or in the case of nonequidistant sampling with favorable sampling density compensation. An NFFT and an adjoint NFFT were used, but no sampling density compensation or explicit regularization.

The conic function shown in Fig. 5.12 is chosen as object to illustrate gridding with a 2D example. Its Fourier transform is given by

$$s(k_r) = \begin{cases} \pi^2 \frac{J_1(Rk_r)H_0(Rk_r) - J_0(Rk_r)H_1(Rk_r)}{k_r^2}, & k_r \neq 0 \\ \frac{1}{3}\pi R^2, & \text{otherwise} \end{cases}, \qquad (5.68)$$

where J_0 and J_1 denote zeroth and first order Bessel functions of the first kind and H denotes the Struve function [28].

Applying an IFFT for reference and a gridding to an equidistant sampling of s with k_x and k_y in the range $[-\frac{1}{4}, \frac{1}{4})$ and $M = 400^2$ results in the errors plotted in Fig. 5.13. The errors are dominated by ringing artifacts at $r_x^2 + r_y^2 = 320^2$ and at the origin, where the conic function is not differentiable. Additional errors introduced by the gridding remain negligible, even though they are perceptibly higher than in the 1D example. The gridding requires about 2.75 times the number of floating point operations of the IFFT in this case, of which more than 80% are involved in the transformation due to the oversampling and less than 20% in the convolution.

The same readout gradient as above is assumed to simulate a nonequidistant sampling of s, but the data acquisition is repeated $\lceil \frac{\pi}{2} N \rceil = 1257$ times. The direction of the readout gradient is rotated by a constant angle after each instance, and with it the sampling positions in the 2D k-space. The number of instances is selected such that the distance between adjacent sampling positions in azimuthal direction does not exceed $\frac{1}{N}$. Thus, subsampling is avoided. The resulting sampling patterns, which
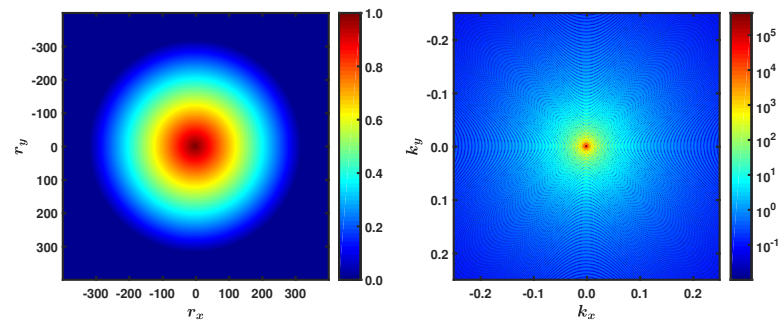
FIGURE 5.12 **2D Object**

A continuous conic function, covering 50% of the square and 64% of the inscribed circular FOV, serves as 2D object (left). The magnitude of its frequency spectrum is displayed with a logarithmic scale (right).
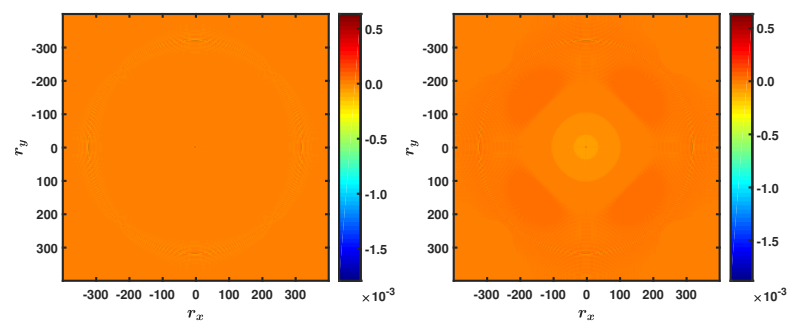

FIGURE 5.13 **2D Cartesian Sampling - IFFT versus Gridding**

From an equidistant sampling of the frequency spectrum in Fig. 5.12, 2D objects are reconstructed with twice the spatial resolution using zero padding, once with an IFFT (left) and once with a gridding (right), and the errors to the continuous conic function are calculated.

cover a circular k-space area, are shown in Fig. 5.8, where the seemingly continuous sampling in azimuthal direction is due to the high density of sampling positions in the k-space center.

Applying a gridding and an iterative reconstruction to the nonequidistant sampling of s produces the errors plotted in Fig. 5.14 and Fig. 5.15, respectively. Weights for sampling density compensation were derived with a geometrical approach and only used in the gridding. Compared to the 1D example, most notably the errors obtained with the gridding in the case of the more realistic gradient system are reduced by one order of magnitude.
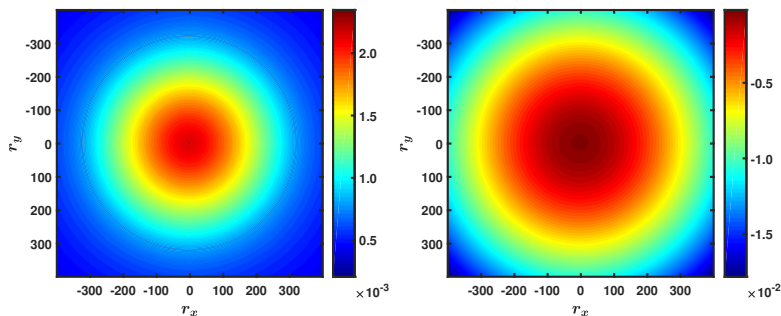
FIGURE 5.14   2D Non-Cartesian Sampling - Gridding

Using the two nonequidistant 2D sampling patterns from Fig. 5.8, 2D objects are reconstructed with twice the spatial resolution with a gridding and the errors to the continuous conic function are calculated.
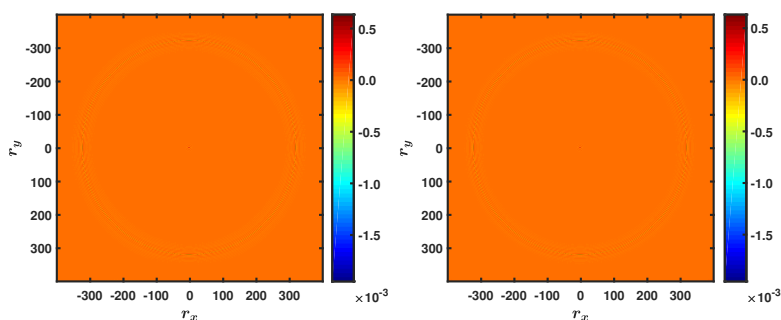

FIGURE 5.15   2D Non-Cartesian Sampling - Iterative Reconstruction

From the two nonequidistant 2D sampling patterns in Fig. 5.8, 2D objects are iteratively reconstructed with twice the spatial resolution and the errors to the continuous conic function are calculated.

The convergence of the iterative reconstruction is analyzed in Fig. 5.16. While using Eq. 5.61 with a sampling density compensation leads to a considerable acceleration compared to using Eq. 5.59 without a sampling density compensation, it adversely affects the convergence in the presence of noise, which demands either a suitable explicit regularization or a sufficiently early termination of the iteration.
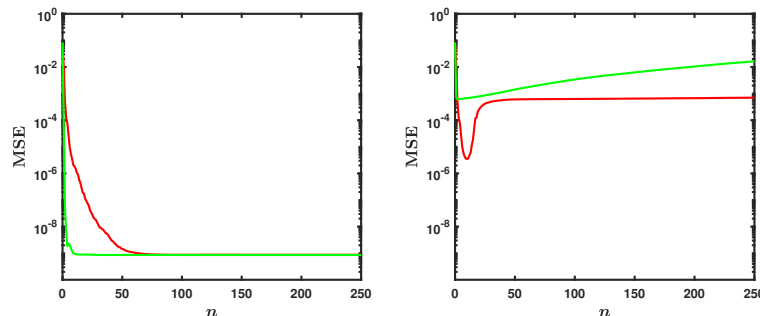
FIGURE 5.16   2D Non-Cartesian Sampling - Convergence

2D objects are iteratively reconstructed without (red) and with (green) sampling density compensation, once without (left) and once with (right) added noise emulating a nominal SNR of 50, and the MSEs to the continuous conic function are plotted as function of the number of iterations.

5.6 SPATIAL RESOLUTION AND NOISE

A common measure of spatial resolution is the full width at half maximum (FWHM) of the main lobe of the PSF. In 1D Cartesian imaging, the PSF is given by Eq. 5.37 and approximated by

$$\text{PSF}(r) \approx \text{sinc}(\pi r) \tag{5.69}$$

for $M = N$ and small $\frac{r}{N}$. The FWHM equals 1.21, since $\text{sinc}(\pi\,0.6) \approx 0.5$. In 2D Cartesian imaging, the PSF remains the same along the axes r_x and r_y, but changes to

$$\text{PSF}(r_d) \approx \text{sinc}^2\left(\frac{\pi}{\sqrt{2}} r_d\right) \tag{5.70}$$

along the diagonals r_d, with $r_d = \pm\sqrt{2}\, r_x$ and $r_x = \pm r_y$, assuming a square k-space area to be covered by the acquisition. The FWHM increases to 1.25, which indicates a slightly anisotropic spatial resolution.

In 2D non-Cartesian imaging, a smaller circular k-space area is usually covered instead, as shown in Fig. 5.1. The PSF is approximated by

$$\text{PSF}(r) \approx 2\,\text{jinc}(\pi r) \tag{5.71}$$

using

$$\text{jinc}(x) = \begin{cases} \frac{J_1(x)}{x}, & x \neq 0 \\ \frac{1}{2}, & \text{otherwise} \end{cases}, \tag{5.72}$$

and the FWHM amounts to 1.41 regardless of direction. Eq. 5.71, as Eq. 5.69 and Eq. 5.70, can be derived by assuming a continuous sampling of the covered k-space
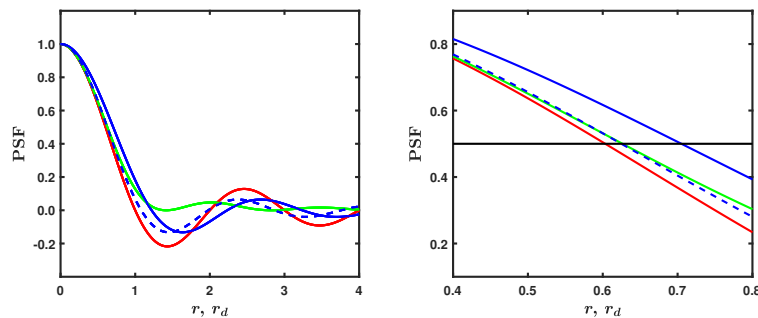
FIGURE 5.17   Spatial Resolution

PSFs are approximated for acquisitions covering a square FOV, along the axes (red) and the diagonals (green), and circular FOVs, with the circle inscribed in the square (solid blue) and the area of the circle and the square equalized (dashed blue), and the crossings of the main lobes with the horizontal line at half the normalized maximum amplitude are determined.

area [29].

To match the spatial resolution in 2D Cartesian imaging, the circular k-space area has to be enlarged relative to the square k-space area. Scaling the radius of the former by $\frac{2}{\sqrt{\pi}} = 1.13$ equalizes the area of both. Applied to Eq. 5.71, this results in

$$\text{PSF}(r) \approx 2 \, \text{jinc}(2 \, \sqrt{\pi} r). \tag{5.73}$$

The FWHM then corresponds to the FWHM along the diagonals in 2D Cartesian imaging. This is illustrated in Fig. 5.17, in which the PSFs according to Eq. 5.69, Eq. 5.70, Eq. 5.71 and Eq. 5.73 are plotted. It is worth noting that the amplitudes of the first side lobes of the PSF along the axes in 2D Cartesian imaging are the highest. In general, this leads to more pronounced ringing artifacts than in 2D non-Cartesian imaging.

The validity of the continuous sampling approximation is substantiated in Fig. 5.18. Despite the rather small number of samples, the calculated PSFs for PRO-PELLER, radial, and spiral imaging and a gridding with sampling density compensation closely agree with each other, to the extent that they are not discernible at this scale, and with the approximated PSF in Fig. 5.17. The calculated and approximated PSFs for EPI along the axes and the diagonals are similarly consistent. Naturally, this only holds for the main lobe and the first side lobes.

While the sampling density compensation is crucial to shape the PSF in gridding, it entails a reduction in SNR by a factor of

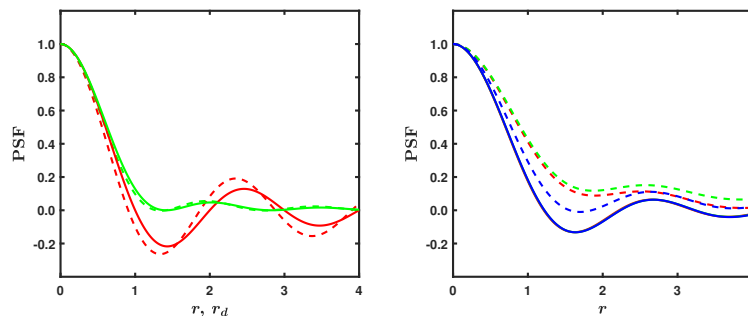$$\frac{\sum_{m=1}^{M} [\mathbf{w}]_m}{\sqrt{M} \, \|\mathbf{w}\|_2}, \tag{5.74}$$

FIGURE 5.18 **Point Spread Functions**

PSFs are calculated for the sampling patterns in Fig. 5.1, namely for EPI along the axes (left, red) and the diagonals (left, green), as well as for PROPELLER (right, red), radial (right, green), and spiral (right, blue) imaging, and a gridding without (dashed) and with (solid) sampling density compensation.

assuming additive white Gaussian noise [30]. This factor equals 1.0 only if the weights are uniform. For the sampling patterns in Fig. 5.1, it decreases to 0.98, 0.85, 0.87, and 0.96 in the case of echo-planar, PROPELLER, radial, and spiral imaging, respectively. It drops further from 0.87 to 0.80 for the second 2D sampling pattern from Fig. 5.8 due to the additional nonequidistant sampling along the projections.

A similar reduction is observed in the right graph in Fig. 5.16 using an iterative reconstruction without sampling density compensation. The nominal SNR of 50 accounts for a mean squared error (MSE) of $4 \cdot 10^{-4}$, given that the maximum signal is normalized to a value of 1.0 and that other errors are negligible. The actual MSE of $6.3 \cdot 10^{-4}$ after 100 iterations then implies an amplification of the noise variance by a factor of 1.58 and a loss in SNR of 20%. However, a CG method provides a diminishing intrinsic regularization in the course of the iterations [31]. This is particularly evident in the right graph in Fig. 5.16 with sampling density compensation. The amplification of the noise variance is ultimately given by the diagonal elements of the matrix

$$\mathbf{X} = \left(\mathbf{E}^{\mathrm{H}}\,\mathbf{E}\right)^{-1} \tag{5.75}$$

or

$$\mathbf{X} = \left(\mathbf{E}^{\mathrm{H}}\,\mathbf{W}\,\mathbf{E}\right)^{-1} \left(\mathbf{E}^{\mathrm{H}}\,\mathbf{W}^2\,\mathbf{E}\right) \left(\mathbf{E}^{\mathrm{H}}\,\mathbf{W}\,\mathbf{E}\right)^{-1} \tag{5.76}$$

and is often unacceptably high without explicit regularization, because the system matrix $\mathbf{E}^{\mathrm{H}}\,\mathbf{E}$ or $\mathbf{E}^{\mathrm{H}}\,\mathbf{W}\,\mathbf{E}$ is typically ill-conditioned in non-Cartesian imaging [26].

Variation in sampling density in k-space also leads to colored noise, which is characterized by a nonconstant power spectral density. Colored noise impairs in particular the perceived spatial resolution in reconstructed images [32]. This can be

mitigated by adding noise or by considering other criteria, for instance for contrast weighting, in the sampling density compensation [33].

5.7 EXTENSIONS

In this chapter, an NFFT for an efficient conversion between equidistant samples in space and nonequidistant samples in k-space was introduced. Its adjoint was shown to be an integral part of a gridding and it and its adjoint of an iterative reconstruction. Other NFFTs exist for related conversions, which are also of relevance to reconstruction in non-Cartesian imaging. They and their applications are briefly discussed in the following.

For a mapping of nonequidistant samples in space to equidistant samples in k-space, the approximation

$$e^{-i2\pi kr} \approx \frac{1}{fN\tilde{c}_{-k}} \sum_{n'=-fN/2}^{fN/2-1} \tilde{c}\left(r - n'\right) e^{-i2\pi kn'} \tag{5.77}$$

is obtained analogously to Eq. 5.11. It leads to the forward model

$$\tilde{s}_m \approx \frac{1}{fN\tilde{c}_{-k_m}} \sum_{n'=-fN/2}^{fN/2-1} \left(\sum_{n=1}^{N} x_n \tilde{c}\left(r_n - n'\right)\right) e^{-i2\pi k_m n'}. \tag{5.78}$$

The inner sum converts the nonequidistant samples in space by a convolution into equidistant samples in space. The outer sum amounts to an FFT of length fN, transforming the equidistant samples in space into equidistant samples in k-space. The deapodization is applied to the equidistant samples in k-space in this case.

Nonequidistant samples in space occur in the presence of an imperfect magnetic field gradient, namely a spatially nonconstant magnetic field gradient, which affects the spatial encoding and leads to distorted images, if it is disregarded in the reconstruction. The signal measured in k-space is modeled by

$$s(k) = \int_{-N/2}^{N/2} x(r)\, e^{-i2\pi kg(r)} dr \tag{5.79}$$

under these circumstances, where g denotes a function mapping the true position r to the apparent position r' in space. Provided that g is invertible, a change in variables results in

$$s(k) = \int_{g(-N/2)}^{g(N/2)} x\left(g^{-1}(r')\right) \frac{dg^{-1}(r')}{dr'}\, e^{-i2\pi kr'} dr' \tag{5.80}$$

and a spatial discretization usually in nonequidistant samples of x. A correction of the distorted images is routinely performed after the reconstruction in space today,

28 **CHAPTER 5** Non-Cartesian MRI Reconstruction

using an interpolation and an intensity scaling. However, integrating it into the reconstruction promises advantages, especially a reduction in the loss of spatial resolution [34]. While this demands an efficient evaluation of Eq. 5.78 in Cartesian imaging, the forward model has to be generalized to nonequidistant samples in both domains in non-Cartesian imaging.

Nonequidistant samples in space also arise from an inhomogeneous main magnetic field. The signal is described by

$$s(t) = \int_{-N/2}^{N/2} x(r)\, e^{-i2\pi k(t)r}\, e^{-i2\pi t f(r)} dr \tag{5.81}$$

in this case. Here, s and k are explicit functions of t, the time after the excitation, and f maps the deviation of the frequency of the precession of the nuclear spins. In Cartesian imaging, k is a linear function of t, because the readout gradient remains unchanged during the acquisition. Thus, Eq. 5.81 can be written as Eq. 5.79 and the same correction can be applied. This still holds in EPI in the phase encoding direction, in which the dominant distortion occurs [35].

The consideration of an inhomogeneous main magnetic field in non-Cartesian imaging in general is discussed in another chapter. Only an NFFT for an efficient conversion between nonequidistant samples in space and nonequidistant samples in k-space is derived here. It is, besides the already introduced NFFTs, applicable to such an off-resonance correction [36, 37]. Instead of approximating the Fourier coefficients of the periodic function $\tilde{c}$, the Fourier transform of the function c

$$(\mathcal{F}c)(r) = \int_{-\infty}^{\infty} c(k)\, e^{-i2\pi kr} dk \tag{5.82}$$

is rewritten as

$$(\mathcal{F}c)(r) = \int_{-1/2}^{1/2} \sum_{p=-\infty}^{\infty} c(k+p)\, e^{-i2\pi(k+p)r} dk \tag{5.83}$$

and approximated by

$$e^{-i2\pi kr} \approx \frac{1}{fN(\mathcal{F}c)(-r)} \sum_{n'=-fN/2}^{fN/2-1} \sum_{p=-\infty}^{\infty} c\left(k - \frac{n'}{fN} + p\right) e^{-i2\pi\left(\frac{n'}{fN}-p\right)r}. \tag{5.84}$$

The inner sum is then eliminated, for example by simply limiting the range of k to $[-\frac{1}{2} + \frac{K}{2fN}, \frac{1}{2} - \frac{K}{2fN})$, leadig to

$$e^{-i2\pi kr} \approx \frac{1}{fN(\mathcal{F}c) - (r)} \sum_{n'=-fN/2}^{fN/2-1} c'\left(k - \frac{n'}{fN}\right) e^{-i2\pi\frac{n'}{fN}r}. \tag{5.85}$$

Such an NFFT also permits including higher order magnetic field perturbations

in the reconstruction, which can be modeled by

$$s(t) = \int_{-N/2}^{N/2} x(r)\, e^{-i2\pi \sum_{l=1}^{L} k_l(t) b_l(r)} dr \qquad (5.86)$$

with spatial basis functions b and corresponding time-variant coefficients k [38]. While spherical harmonics are commonly chosen for b, separate calibration measurements, such as gradient impulse response measurements, or concurrent magnetic field monitoring are usually performed to determine k [39, 40]. Even if only spherical harmonics of first order are considered, which correspond to a spatially constant magnetic field gradient, knowledge of the actual sampling positions in k-space with high accuracy often constitutes a crucial prerequiste for attaining adequate image quality in non-Cartesian imaging.

Finally, exponential signal decay during the acquisition can be incorporated into Eq. 5.81 by adding a scaled relaxation rate as imaginary part to f [41].
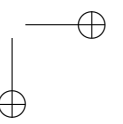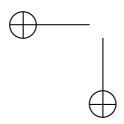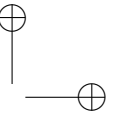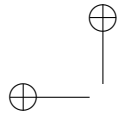
Bibliography

1. Lauterbur PC, Image formation by induced local interactions: Examples employing nuclear magnetic resonance. Nature 1973; 242:190–191.

2. Kumar A, Welti D, Ernst RR, NMR Fourier Zeugmatography. J Magn Reson 1975; 18:69–83.

3. Ernst RR, NMR Fourier Zeugmatography. J Magn Reson 2011; 213:510–512.

4. Mansfield P, Multi-planar image formation using NMR spin echoes. J Phys C 1977; 10:L55–L58.

5. Pipe JG, Motion correction with PROPELLER MRI: Application to head motion and free-breathing cardiac imaging. Magn Reson Med 1999; 42:963–969.

6. Ahn CB, Kim JH, Cho ZH, High-speed spiral-scan echo planar NMR imaging - I. IEEE Trans Med Imaging 1986; 5:2–7.

7. Dutt A, Rokhlin V, Fast Fourier transforms for nonequispaced data. SIAM J Sci Comput 1993; 14:1368–1393.

8. Plonka G, Potts D, Steidl G, Tasche M, Numerical Fourier Analysis. Basel: Birkhäuser, 2019.

9. O'Sullivan JD, A fast sinc function gridding algorithm for Fourier inversion in computer tomography. IEEE Trans Med Imaging 1985; 4:200–207.

10. Jackson JI, Meyer CH, Nishimura DG, Macovski A, Selection of a convolution function for Fourier inversion using gridding. IEEE Trans Med Imaging 1991; 10:473–478.

11. Slepian D, Pollak HO, Prolate spheroidal wave functions, Fourier analysis and uncertainty - I. Bell Syst Tech J 1961; 40:43–63.

12. Kaiser JF, Digital filters. In: Kuo FF, Kaiser JF, editors, System Analysis by Digital Computer, New York: Wiley, 1966; pp. 218–285.

13. Fessler JA, Sutton BP, Nonuniform fast Fourier transforms using min-max interpolation. IEEE Trans Signal Process 2003; 51:560–574.

14. Wajer FTAW, Woudenberg E, de Beer R, Fuderer M, Mehlkopf AF, van Ormondt D, Simple equation for optimal gridding parameters. In: Proceedings of the 7th Annual Meeting of the ISMRM, Philadelphia, Pennsylvania, USA, 1999, p. 663.

15. Beatty PJ, Nishimura DG, Pauly JM, Rapid gridding reconstruction with a minimal oversampling ratio. IEEE Trans Med Imaging 2005; 24:799–808.

16. Dale B, Wendt M, Duerk JL, A rapid look-up table method for reconstructing MR images from arbitrary k-space trajectories. IEEE Trans Med Imaging 2001; 20:207–217.

17. Boada FE, Hancu I, Shen GX, Spherically symmetric kernels for improved convolution gridding. In: Proceedings of the 7th Annual Meeting of the ISMRM, Philadelphia, Pennsylvania, USA, 1999, p. 1654.

18. Brouw WN, Aperture synthesis. In: Alder B, Fernbach S, Rotenberg M, editors, Methods in Computational Physics, Vol. 14, New York: Academic, 1975; pp. 131–175.

19. Hoge RD, Kwan RKS, Pike GB, Density compensation functions for spiral MRI. Magn Reson Med 1997; 38:117–128.

20. Rasche V, Proksa R, Sinkus R, Börnert P, Eggers H, Resampling of data between arbitrary grids using convolution interpolation. IEEE Trans Med Imaging 1999; 18:385–392.

21. Rosenfeld D, An optimal and efficient new gridding algorithm using singular value decomposition. Magn Reson Med 1998; 40:14–23.

22. Sedarat H, Nishimura DG, On the optimality of the gridding reconstruction algorithm. IEEE Trans Med Imaging 2000; 19:306–317.

23. Pipe JG, Menon P, Sampling density compensation in MRI: Rationale and an iterative numer-

32   Bibliography

ical solution. Magn Reson Med 1999; 41:179–186.

24. Wajer FTAW, Pruessmann KP, Major speedup of reconstruction for sensitivity encoding with arbitrary trajectories. In: Proceedings of the 9th Annual Meeting of the ISMRM, Glasgow, Scotland, 2001, p. 767.

25. Eggers H, Boernert P, Boesiger P, Comparison of gridding- and convolution-based iterative reconstruction algorithms for sensitivity-encoded non-Cartesian acquisitions. In: Proceedings of the 10th Annual Meeting of the ISMRM, Honolulu, Hawai'i, USA, 2002, p. 743.

26. Pruessmann KP, Weiger M, Börnert P, Boesiger P, Advances in sensitivity encoding with arbitrary k-space trajectories. Magn Reson Med 2001; 46:638–651.

27. Johnson KO, Pipe JG, Convolution kernel design and efficient algorithm for sampling density correction. Magn Reson Med 2009; 61:439–447.

28. Abramowitz M, Stegun IA, editors, Handbook of Mathematical Functions with Formulas, Graphs, and Mathematical Tables. New York: Dover, 1972.

29. Lauzon ML, Rutt BK, Effects of polar sampling in k-space. Magn Reson Med 1996; 36:940–949.

30. Pipe JG, Duerk JL, Analytical resolution and noise characteristics of linearly reconstructed magnetic resonance data with arbitrary k-space sampling. Magn Reson Med 1995; 34:170–178.

31. Qu P, Zhong K, Zhang B, Wang J, Shen GX, Convergence behavior of iterative SENSE reconstruction with non-Cartesian trajectories. Magn Reson Med 2005; 54:1040–1045.

32. Newbould R, Liu C, Bammer R, Colored noise and effective resolution: Data considerations for non-uniform k-space sampling reconstructions. In: Proceedings of the 14th Annual Meeting of the ISMRM, Seattle, Washington, USA, 2006, p. 2939.

33. Eggers H, van Yperen GH, Nehrke K, Contrast optimization by data weighting in PROPELLER imaging. In: Proceedings of the 15th Annual Meeting of the ISMRM, Berlin, Germany, 2007, p. 1737.

34. Tao S, Trzasko JD, Shu Y, Huston III J, Bernstein MA, Integrated image reconstruction and gradient nonlinearity correction. Magn Reson Med 2015; 74:1019–1031.

35. Jezzard P, Balaban RS, Correction for geometric distortion in echo planar images from B_0 field variations. Magn Reson Med 1995; 34:65–73.

36. Sutton BP, Noll DC, Fessler JA, Fast, iterative image reconstruction for MRI in the presence of field inhomogeneities. IEEE Trans Med Imaging 2003; 22:178–188.

37. Eggers H, Knopp T, Potts D, Field inhomogeneity correction based on gridding reconstruction for magnetic resonance imaging. IEEE Trans Med Imaging 2007; 26:374–384.

38. Wilm BJ, Barmet C, Pavan M, Pruessmann KP, Higher order reconstruction for MRI in the presence of spatiotemporal field perturbations. Magn Reson Med 2011; 65:1690–1701.

39. Alley MT, Glover GH, Pelc NJ, Gradient characterization using a Fourier-Transform technique. Magn Reson Med 1998; 39:581–587.

40. de Zanche N, Barmet C, Nordmeyer-Massner JA, Pruessmann KP, NMR probes for measuring magnetic fields and field dynamics in MR systems. Magn Reson Med 2008; 65:176–186.

41. Knopp T, Eggers H, Dahnke H, Prestin J, Sénégas J, Iterative off-resonance and signal decay estimation and correction for multi-echo MRI. IEEE Trans Med Imaging 2009; 28:394–404.